



Delft University of Technology

Three-dimensional localization microscopy with increased axial precision through TIRF angle modulation

Fan, Daniel; Cnossen, Jelmer; Hung, Shih Te; Kromm, Dimitri; Dekker, Nynke H.; Verbiest, Gerard J.; Smith, Carlos S.

DOI

[10.1016/j.optcom.2023.129548](https://doi.org/10.1016/j.optcom.2023.129548)

Publication date

2023

Document Version

Final published version

Published in

Optics Communications

Citation (APA)

Fan, D., Cnossen, J., Hung, S. T., Kromm, D., Dekker, N. H., Verbiest, G. J., & Smith, C. S. (2023). Three-dimensional localization microscopy with increased axial precision through TIRF angle modulation. *Optics Communications*, 542, Article 129548. <https://doi.org/10.1016/j.optcom.2023.129548>

Important note

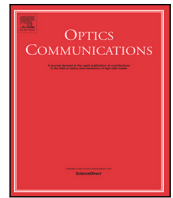
To cite this publication, please use the final published version (if applicable).
Please check the document version above.

Copyright

Other than for strictly personal use, it is not permitted to download, forward or distribute the text or part of it, without the consent of the author(s) and/or copyright holder(s), unless the work is under an open content license such as Creative Commons.

Takedown policy

Please contact us and provide details if you believe this document breaches copyrights.
We will remove access to the work immediately and investigate your claim.



Three-dimensional localization microscopy with increased axial precision through TIRF angle modulation

Daniel Fan^{a,1}, Jelmer Cnossen^{a,1}, Shih-Te Hung^a, Dimitri Kromm^a, Nynke H. Dekker^b, Gerard J. Verbiest^c, Carlas S. Smith^{a,*}

^a Delft Center for Systems and Control, Faculty of Mechanical, Maritime, and Materials Engineering, Technische Universiteit Delft, Mekelweg 2, Delft, 2628CD, Zuid-Holland, The Netherlands

^b Department of Bionanoscience, Kavli Institute of Nanoscience Delft, Technische Universiteit Delft, Van der Maasweg 9, Delft, 2629HZ, Zuid-Holland, The Netherlands

^c Department of Precision and Microsystems Engineering, Faculty of Mechanical, Maritime, and Materials Engineering, Technische Universiteit Delft, Mekelweg 2, Delft, 2628CD, Zuid-Holland, The Netherlands

ARTICLE INFO

Keywords:

Super-resolution microscopy
Total internal reflection fluorescence
TIRF microscopy
PSF engineering
Single molecule localization microscopy

ABSTRACT

To better understand the interactions between biological molecules, a high optical resolution in all three dimensions is crucial. The intrinsically lower axial resolution of microscopes however, is a limiting factor in fluorescence imaging, correspondingly in fluorescence based single molecule localization microscopy (SMLM). Here, we present a method to improve the axial localization precision in SMLM by combining point-spread-function engineering with total internal reflection fluorescence (TIRF) fields with decay lengths that vary within the on-time of a fluorophore. Such time-varying illumination field intensity allows one to extract additional axial location information from the emitted photons. With this time varying illumination approach, we show that axial localization is improved two-fold over TIRF-based SMLM using astigmatic PSFs. We calculate theoretical resolution gains for various imaging conditions via the Cramér Rao Lower Bound (CRLB), a commonly used metric to compute the best attainable localization precision in SMLM.

1. Introduction

Single molecule localization microscopy (SMLM) has breached the optical diffraction limit and thereby allowed insights into the features of sub-cellular structures [1–3]. Although the lateral localization precision has reached the single-digit-nm level [4], similar axial precision is needed to unravel the interactions between bio-molecules in a 3D environment.

Using high numerical aperture (NA) optics combined with point-spread-function (PSF) engineering [5], the axial resolution is approximately three times worse than lateral resolution (i.e., typically 15 nm). At this resolution, for example, the hollow structure of microtubules is difficult to resolve in 3D [6]. Further improvements using multiple objectives to record emission interference requires complex instrument alignment [7], while Förster resonance energy transfer (FRET) and metal induced energy transfer (MIET) [8] localization require complex data analysis to overcome low signal-to-noise ratios [9,10]. The use of illumination patterns in the axial direction [6,11,12] and emitter self-interference [13] has produced axial resolution improvements with less exacting experimental setups compared to multiple-objective systems.

Nevertheless, the aforementioned methods utilize widefield or highly inclined illumination of the sample, compromising the desirable optical sectioning that is a crucial aspect for practical application of SMLM in biologically relevant samples.

The commonly employed methods to achieve sufficient optical sectioning and thereby limiting photobleaching and improving the signal-to-noise ratio are light sheet microscopy [14,15] and total internal reflection fluorescence (TIRF) [16]. Light sheet microscopy employs a narrow sheet of light to selectively illuminate a thin layer of the sample, typically a few microns in thickness. TIRF microscopy makes use of the evanescent field produced at the interface of two media to only excite fluorophores within a depth of 300 nm from the coverslip. Due to the limited excitation depth, TIRF microscopy has been primarily used to study events at the cell surface, such as live cell-cell interactions [17], endo- and exocytosis [18,19], cytoskeletal dynamics [20], etc. TIRF excitation occurs at the low refractive index side of an interface when light strikes the high refractive index side at or above the critical incidence angle (Fig. 1a). Practically, the incident light beam can propagate via a high-NA objective (Fig. 1b), via prism

* Corresponding author.

E-mail address: C.S.Smith@tudelft.nl (C.S. Smith).

¹ Authors contributed equally.

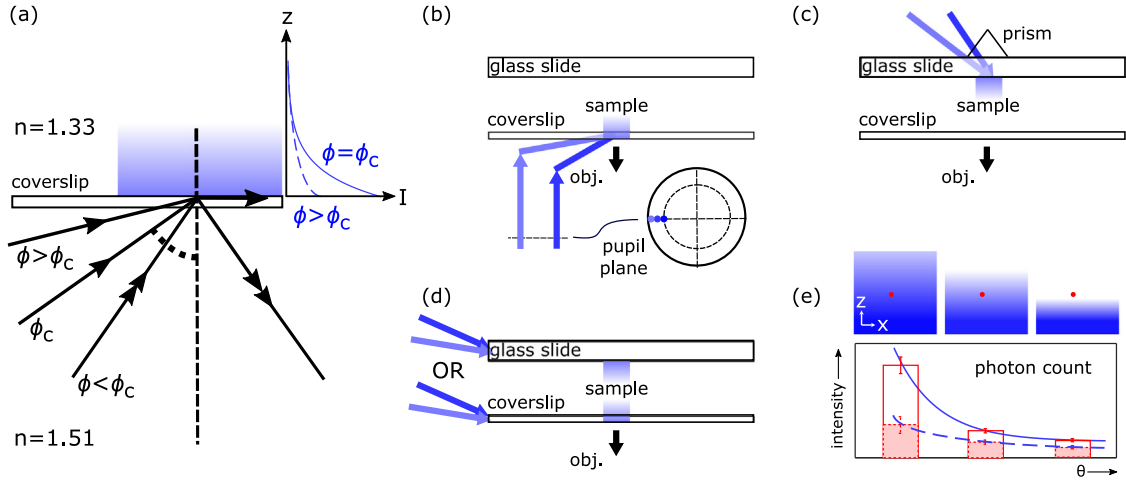


Fig. 1. Schematic of method. (a) Scheme of standard TIRF microscopy where an evanescent field is produced when the illumination angle on the high-refractive index side is above the critical angle. The illumination evanescent field intensity decays exponentially perpendicular to the interface. For TIRFscan, the TIRF illumination field intensity at the coverslip or at the glass slide surface is scanned either (b) at the back focal plane of a high-NA objective, (c) via a prism on top of the glass slide, or (d) via waveguides built into the coverslip or glass slide. (e) The emitted photon counts (red) can then be fitted (blue solid line) according to the decaying TIRF illumination field intensities (shaded blue), resulting in a better fit for the axial position of the emitter. Different emitters at different z -positions would have different dependencies between TIRF angle and emitted intensity (blue solid vs. dotted line). Error bars represent typical experimental error in emitter intensity.

coupling [21] (Fig. 1c), or via a waveguide [22] (Fig. 1d). Objective-type TIRF has the benefit of TIRF excitation and imaging close to the coverslip, avoiding the through-the-sample focusing that occurs in prism TIRF. However, the use of objective-type TIRF can result in non-ideal TIRF fields either due to inaccurate optical alignment at the back focal plane and/or light scattering through the optical system involving complex high-NA elements. Residual laser modes also have a pronounced effect which degrades the TIRF field's quality and become amplified via the high NA and high magnification objective lens [21,23]. Such spurious modes can lead to a mixture of TIRF fields, decreasing the overall sectioning capability due to the mixture of decay lengths [24]. Waveguide-based TIRF requires custom sample holders and coverslips [22], but overall both waveguide-type TIRF and prism-type TIRF deliver cleaner, more ideal TIRF fields than objective-type TIRF [21,23,25]. In TIRF microscopy, the illumination field intensity becomes exponentially smaller along the axial direction, an effect that depends on the present refractive indices, the excitation wavelength, as well as the light's incident angle (see theory section). Therefore, previous studies exploited the angle-dependence of the illumination profile to determine the axial positions of fluorophore distributions via excitation under varying angles [26–29]. Such techniques are commonly referenced as variable angle TIRF microscopy [30] and rely on an a priori calibration model to determine the axial position of the emission. Recently, in order to combine TIRF microscopy with the axial localization of single emitters, the modeling and accurate calibration of illumination and emission intensities [30–32] were used. In these approaches, the TIRF illumination field intensity is measured using a calibration sample [30] or the emitted evanescent intensity is modeled [31,32]. Using this information, measurements of the actual emitter intensity can provide axial information. However, a disadvantage of this approach is that the calibration measurement conditions must be the same as that of the specimen.

Here, we introduce a new method to improve the axial localization precision using TIRF microscopy without the need for calibration samples or complex customized instrumentation. In terms of hardware it requires a relatively straightforward modification of a standard TIRF microscope with astigmatic imaging (whether it be objective-type, prism-type, or waveguide-type TIRF).

Since the evanescent field at the coverslip arising from TIRF illumination decays at different rates in the z -direction depending on the incidence angle, the z -location of an emitter can be deduced from its

emission intensity under illumination at different TIRF angles. Combined with conventional astigmatic imaging, the use of a sequentially changing TIRF field (hereafter called TIRFscan) within the “on” time of an emitter (i.e., tens to hundreds of milliseconds) roughly doubles the axial localization precision.

2. Theory

In this theoretical study, we use regular TIRF microscopy with an astigmatic PSF as a benchmark. We compare how TIRFscan combined with astigmatic imaging versus astigmatic imaging alone perform in SMLM, with focus on the axial direction. In principle, TIRFscan can offer precision improvement combined with any suitable axial localization scheme, including super-resolution imaging without any PSF engineering. However, for TIRFscan combined with imaging using Gaussian PSFs alone, the absolute Cramér Rao Lower Bound (CRLB) can reach infinity close to the focal plane, making it a bad choice for benchmarking. Therefore, we combine with astigmatic imaging as it is a simple, robust, and widely used method for axial localization and offers a suitable benchmark for comparison of axial precision. The comparison is in terms of the theoretical CRLB, i.e. the theoretical axial limit. No estimators were implemented in this work, although the Levenberg–Marquardt algorithm has been shown to reach the CRLB for astigmatic imaging alone [33,34]. This can be done, for example, by fitting the expected pixel value to the imaging model [35].

2.1. The imaging model

Total internal reflection, and subsequently an evanescent wave occur at the interface of two media of different refractive index, when light is incident at the high refractive index side (in TIRF microscopy typically immersion oil with $n_1 \approx 1.51$) with an incidence angle ϕ at or beyond the critical angle. The evanescent field will then be present in the medium with lower refractive index (typically water with $n_2 \approx 1.33$) with a decay length d_ϕ perpendicular to the interface:

$$d_\phi = \frac{\lambda_i}{4\pi \sqrt{n_1^2 \sin^2 \phi - n_2^2}}, \quad (1)$$

where λ_i is the incidence wavelength. Assuming an incident plane wave, the illumination evanescent field's intensity I_ϕ on the specimen side as a function of axial distance from coverslip z will then be:

$$I_\phi(z) = I_\phi(0) \left(\alpha \exp\left(-\frac{z}{d_\phi}\right) + 1 - \alpha \right), \quad (2)$$

where $I_\phi(0)$ is the intensity at the coverslip of the evanescent field on the sample side and α represents the linear stray light illumination component coming from within the optical system [30].

For objective-type TIRF, α typically lies between 0.9 and 1, as scattering within the optical system (which includes complex high-NA optics) together with the magnification of unclear laser profiles by high-NA optics can result in non-ideal TIRF fields. For waveguide and prism-based TIRF, the value of α is closer to 1, as these TIRF fields are typically cleaner [21].

For normal TIRF imaging, only one TIRF angle equivalent to a certain decay length is used. If multiple known TIRF angles, i.e., known decay lengths, are used for the same emitter, its measured emission intensity at each angle can be used to further improve the axial localization precision (Fig. 1e). This is similar to other patterned illumination schemes [4,6,12,34], where precise knowledge of the illumination pattern helps pinpoint and further improve the localization precision of an emitter by emission intensity measurement.

Here, we use the CRLB, a lower bound on the variance of unbiased estimators [36], to show that TIRFscan indeed improves the axial localization precision. Starting with the astigmatic imaging model from Ref. [33], the form of the 3D astigmatic PSF on the camera is:

$$PSF(x, y, \theta_x, \theta_y, \theta_z) = \frac{1}{2\pi\sigma_x(\theta_z)\sigma_y(\theta_z)} e^{-\frac{(x-\theta_x)^2}{2\sigma_x(\theta_z)^2} - \frac{(y-\theta_y)^2}{2\sigma_y(\theta_z)^2}}, \quad (3)$$

where x, y are the camera pixel centers, $\theta_x, \theta_y, \theta_z$ is the emitter position, and the standard deviations are:

$$\sigma_x(\theta_z) = \sigma_{0x} \sqrt{1 + \frac{(\theta_z - \gamma_x)^2}{D_x^2} + A_x \frac{(\theta_z - \gamma_x)^3}{D_x^2}}, \quad (4)$$

$$\sigma_y(\theta_z) = \sigma_{0y} \sqrt{1 + \frac{(\theta_z + \gamma_y)^2}{D_y^2} + A_y \frac{(\theta_z + \gamma_y)^3}{D_y^2}}, \quad (5)$$

with σ_0, γ, D , and A being fitting parameters for the x and y directions. These values are taken from the PSF model produced from [37] using an illumination wavelength of 640 nm and emission wavelength of 680 nm (details of the model parameters are provided in the supplementary Python scripts). The expected photon counts μ_k of the k th pixel of a detector centered at (x_k, y_k) is thus, given an illumination field intensity $I_{\phi_n}(\theta_z)$ with a TIRF angle ϕ_n :

$$\mu_{kn} = I_{\phi_n}(\theta_z) \left(\theta_1 h_k(\theta_x, \theta_y, \theta_z) + \theta_{bg_n} \right), \quad (6)$$

with

$$h_k = \int_{A_k} PSF(u, v, \theta_x, \theta_y, \theta_z) dudv, \quad (7)$$

where PSF is integrated over the finite area A_k of the k th pixel of the detector [33]. The functional dependence on the estimands of μ_k has been omitted for convenience of shorthand notation. Furthermore, θ_{bg_n} is the normalized background, which enables a quantitative comparison between different numbers of illumination intensities (N).

2.2. The normalized background

The integrated background (bg) at a particular TIRF angle ϕ_n is:

$$bg_n = \theta_{bg_n} \int_0^\infty I(\theta_z) d\theta_z = \theta_{bg_n} d_{\phi_n} I(0)\alpha, \quad (8)$$

where the scattering contribution $(1 - \alpha)$ is assumed to be constant for all TIRF angles and cancels out during normalization. The fraction of background at a particular TIRF angle with respect to the other angles is:

$$\frac{bg_n}{\sum_{n=1}^N bg_n} = \frac{\theta_{bg_n} \alpha I(0) d_{\phi_n}}{\theta_{bg_n} \alpha I(0) \sum_{n=1}^N d_{\phi_n}} = \frac{d_{\phi_n}}{\sum_{n=1}^N d_{\phi_n}} \quad (9)$$

Therefore, we define the normalized background as:

$$\theta_{bg_n} = \theta_{bg} \frac{d_{\phi_n}}{\sum_{n=1}^N d_{\phi_n}} \quad (10)$$

2.3. The localization precision

The Fisher information matrix with elements F_{ij} , is then calculated for either a single ($N = 1$) or multiple illumination intensities ($N > 1$):

$$F_{ij} = \sum_{n=1}^N \sum_{k=1}^K \frac{1}{\mu_{kn}} \frac{\partial \mu_{kn}}{\partial \theta_i} \frac{\partial \mu_{kn}}{\partial \theta_j} \quad (11)$$

The optimal estimation precision of the i -th parameter is:

$$\sigma_i = \sqrt{[F^{-1}]_{ii}}, \quad (12)$$

where $[.]_{ii}$ is the i th diagonal element of the CRLB. Closed-form expressions for these derivatives are easily computed [33].

3. Results

To evaluate the localization precision gain of TIRFscan over standard 3D SMLM relying on astigmatic imaging, we estimated the best achievable localization precision based on the CRLB calculation presented above. In the process, we chose various optical configurations to represent possible experimental conditions. As a basis we used a TIRF objective with NA = 1.49, with a total emitted intensity of 1000 photons per region of interest and background of 10 photons per pixel. The illumination wavelength was set at 640 nm and emission wavelength at 680 nm. The focal plane was kept at the coverslip ($\theta_z = 0$) in all cases. All TIRFscan calculations kept the same total photon budget distributed over the TIRFscan angles. An astigmatic PSF model was generated for NA = 1.49 and used throughout the calculations except where otherwise stated (the parameters for PSF model generation are attached in the supplementary Python scripts) [37].

Fig. 2a shows the axial CRLB within 300 nm of the coverslip for astigmatic imaging alone (black solid line) versus TIRFscan using multiple TIRF angles. An approximate two-times improvement is observed by using two scanning angles (darkest purple line). Using three or more scanning angles improved the CRLB beyond 150 nm distance from the coverslip. Within 150 nm from the coverslip the CRLB increases by a marginal amount with respect to only two scanned angles. This is likely due to the combination of angle dependent penetration depth, limited photon budget and signal-to-noise ratio.

Non-ideal experimental parameters for objective based TIRF, including previously mentioned concerns such as optical scattering, unclear laser modes, and optical alignment, were also calculated to show technical feasibility (see Fig. 2b–d). The improvement factor, when varying the minimum (solid lines) and maximum (dotted lines) TIRF angles for 2-angle TIRFscan, is shown in Fig. 2b. For small deviations of the angles around their maximum and minimum, we find that the 2nd angle consistently improves the localization precision by at least 50% until a depth of ~200 nm. Fig. 2c shows the effect of non-evanescent illumination contributions from scattered light due to microscope optics [30]. Typical values given in [30] are $\alpha \sim 0.9 - 0.95$. In this range the improvement factor drops but is still between 1.5 and 2. Fig. 2d compares 2 angle TIRFscan for an NA = 1.49 objective and an NA = 1.7 objective, under varying experimental conditions. The additional angle range provided by the higher NA objective leads to improvement factors around 3 near the sample which quickly drops compared with the lower NA case. Interestingly, it is around the ~150 nm mark, that the lower NA illumination starts to provide better localization precision. This is likely due to the angle dependent penetration depth of the evanescent field, which results in weaker signals at greater depths for larger incident angles. For the NA = 1.7 objective, the astigmatic PSF model was re-calculated using [37] although there was little difference in improvement factor.

For waveguide and prism TIRF, the higher refractive index medium can be decoupled from the objective and immersion oil, while smaller optical scattering factors and relaxed alignment tolerances result in cleaner TIRF fields (i.e., $\alpha = 1$) closer to the critical angle. Fig. 3a and

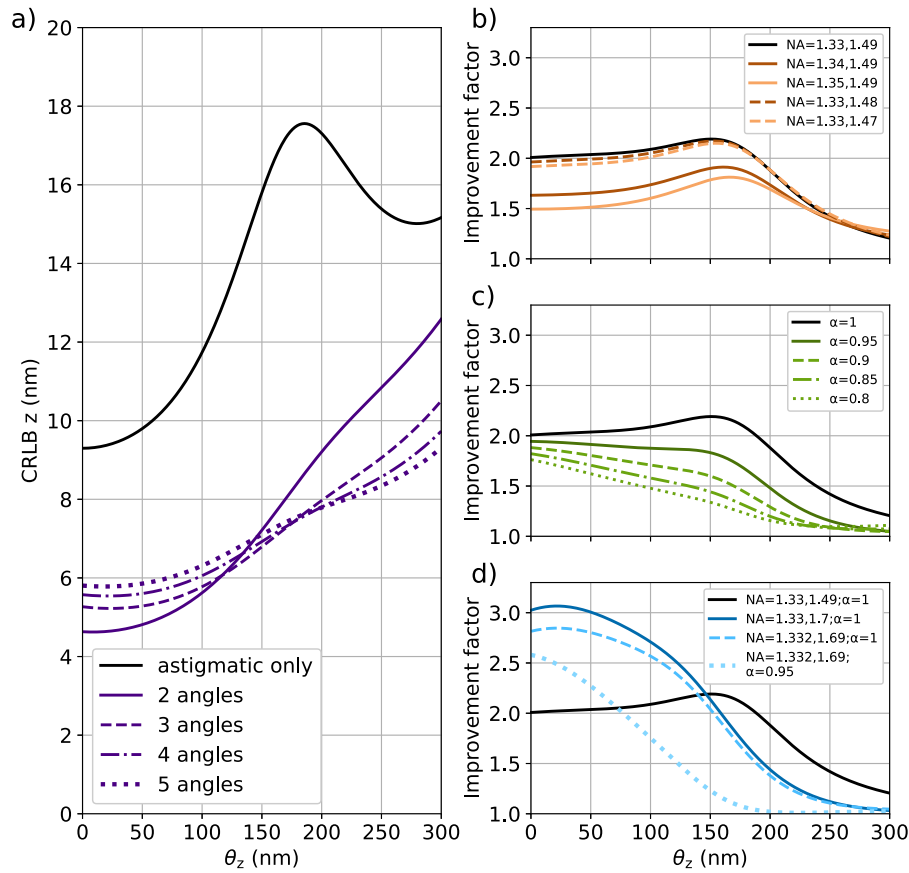


Fig. 2. TIRFscan CRLB and improvement factor for objective based TIRF (a) True axial position vs. CRLB of axial position of astigmatic imaging only (black) compared with TIRFscan comprising different numbers of angles. 2 angles (darkest purple): NA = 1.33, 1.49; 3 angles: NA = 1.33, 1.41, 1.49; 4 angles: NA = 1.33, 1.38, 1.44, 1.49; 5 angles (lightest purple): NA = 1.33, 1.37, 1.41, 1.45, 1.49. Improvement factor of TIRFscan with (b) two angles where the minimum and maximum angles are varied; (c) with two angles (NA = 1.33, 1.49) and different α ; (d) with two angles and using an NA = 1.49 TIRF objective versus an NA = 1.7 TIRF objective. In all cases the focal plane was at $z = 0$ nm.

b show that by using TiO_2 waveguides ($n = 2.5$, dotted lines) [25] a possible 4–6 times improvement factor (corresponding to 1.7–2.5 nm precision) can be reached, albeit close to the interface. Use of sapphire ($n = 1.78$, dashed lines), a common optical material, improves the CRLB by a factor of ~ 3 within the first 200 nm from the interface. In all cases, the CRLB improvement drops after 200 nm from the interface, and in general drops (dotted lines) with stray scattered light (Fig. 3c).

Lastly, note that in this benchmarking study of the effects of various schemes of TIRFscan compared with astigmatic imaging, a suitable focal plane was chosen, fixed at the coverslip. For measurements, this can be tuned depending on the measurement in order to improve the absolute CRLB. For example, Fig. 4 shows the CRLB and improvement factor using two TIRF angles (NA = 1.33 and 1.49) with $\alpha = 1$ for a focal plane at 0, 150, 300, and 750 nm above the coverslip. Adjusting the focal plane would allow the improvement factor to be optimized across the range of interest. Note that the intensity has been normalized to 1000 photons for a fair comparison between the various schemes. In practice this would mean adjusting the laser power, at the cost of changing the fluorophore emission time and potentially damaging and/or bleaching the specimen. For an exponentially decaying TIRF field, the maximum practical focal plane distance away from the coverslip is quickly reached. Furthermore, although fluorophores away from the coverslip can appear to have similar improvement factor (e.g. Fig. 4c, focal plane at 300 nm), the absolute CRLB is often worse (Fig. 4b, focal plane at 300 nm vs. 150 nm).

4. Discussion and conclusions

In this study, we have presented a novel technique based on multiple angle TIRF illumination (TIRFscan) and shown the localization

precision gains under various conditions theoretically. The improvement factors have been simulated with the help of the CRLB, and tested for different angles, number of angles, and scattering. For objective-type TIRFscan (Fig. 2), 2 angle scanning is sufficient to show large axial localization improvement. Further, the minimum angle (minimum angles NA = 1.34 and NA = 1.35, Fig. 2b, solid lines) should be as close as possible to the critical angle, while variations in maximum angle (maximum angles NA = 1.47 and NA = 1.48, Fig. 2b, dotted lines) have much less effect ($< 10\%$) on the improvement factor.

Contrary to the maximum angle, the optical scattering factor α can have a significant effect on the CRLB (Fig. 2c) where non-evanescent illumination field intensity can decrease the localization precision of TIRFscan. For an objective with NA = 1.49 and $\alpha > 0.85$, we expect improvement factors > 1.5 within the first 150 nm depth, peaking at an improvement of ~ 2.3 for $\alpha = 1.0$.

Using a high-NA objective (e.g., NA = 1.7) shows a CRLB improvement by a factor of 3 in the first 50 nm, and drops off rapidly thereafter (Fig. 2d) as at large TIRF angles the decaying evanescent illumination field intensity drops rapidly to zero. High-NA objectives also require the use of volatile immersion oils which may introduce toxicity and autofluorescence, as well as the use of special cover slips such as sapphire which are expensive [38,39]. Further, at small distances (~ 3 nm), fluorophore cross-talk can affect precision [40], and needs to be considered.

More realistic optical scattering and alignment factors show a rapid drop in CRLB (Fig. 2b–c) which has consequences for the practical implementation: In order to minimize the scattering factor α , we recommend the angle scanning in combination with prism-type TIRF or waveguide-type TIRF. Another practical consideration stems from TIRFscan's requirement for the fluorophore to be “on” during the

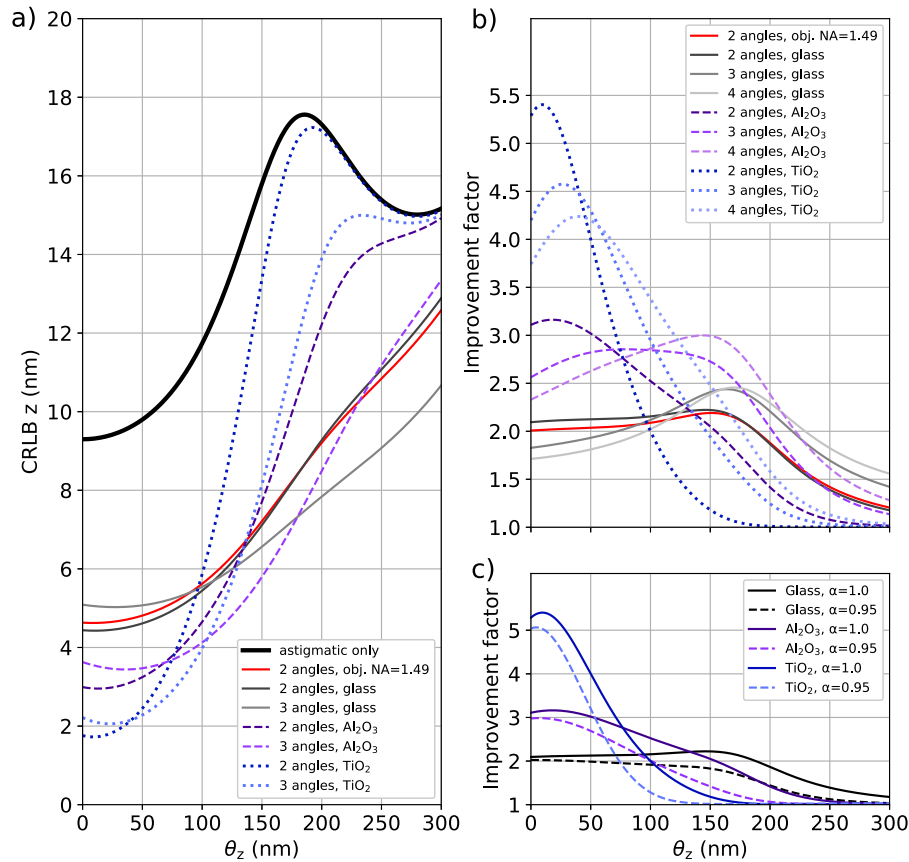


Fig. 3. TIRFscan CRLB and improvement factor for prism and waveguide based TIRF (a) CRLB and (b) improvement factor for 2, 3, and 4 TIRFscan angles where the high refractive index medium is glass ($n = 1.51$), Al_2O_3 ($n = 1.78$), or TiO_2 ($n = 2.5$). These are relevant for waveguide and prism TIRF where different materials can be used. In all cases $\alpha = 1$. For glass, 2 angles: NA = 1.33, 1.51; 3 angles: NA = 1.33, 1.42, 1.51; 4 angles: NA = 1.33, 1.39, 1.45, 1.51. For Al_2O_3 , 2 angles: NA = 1.33, 1.78; 3 angles: NA = 1.33, 1.555, 1.78; 4 angles: NA = 1.33, 1.48, 1.63, 1.78. For TiO_2 , 2 angles: NA = 1.33, 2.5; 3 angles: NA = 1.33, 1.915, 2.5; 4 angles: NA = 1.33, 1.72, 2.11, 2.5. For comparison, objective TIRFscan with 2 angles NA = 1.33, 1.49 is shown as a red line. (c) Effect of non-ideal α factor ($\alpha = 0.9$ vs $\alpha = 1$).

excitation process under each angle. In turn, fast scanning, e.g. via a galvanometric mirror or optical modulator, is required. Therefore, potentially short fluorophore on-times would encourage the use of a minimum number of scanning angles.

While technically challenging, we are confident that an experimental realization of a microscope, which records multiple frames for multiple excitation angles, can be realized. Structured illumination approaches that require dyes to emit photons at similar brightness levels over multiple frames and illumination patterns have shown recently that this is technically and computationally feasible [12,34,41]. In one of these studies for example, 6 illumination patterns per on-cycle of the emitter are recorded and only a moderate amount of localizations are discarded, i.e. $\leq 30\%$ [34]. As already 2 varied angles can lead to an improvement in the CRLB over sole astigmatic PSF localization, the estimator algorithm can be designed to only account for emission that satisfies the expected intensity changes that correspond to the on-time of the emitter. Ergo, emitters that satisfy the condition, can be fitted for the amount of angles during which they remained on. Emitters that showed an interruption in emission on the other hand, will be rejected or only fitted to the number of angles during which they satisfied the on-condition. Additionally, if needed, the camera acquisition can run at a faster rate than the TIRF angle change. Having multiple camera frames per TIRF angle allows to further improve rejection of emitters that are only partially on during the TIRF angle scan.

Depending on the imaging depth, we showed, that in two angle TIRFscan it can be beneficial to change the excitation angles to

maintain higher localization precision, e.g. beyond 150 nm depth a maximum NA of 1.49 achieves a higher improvement factor than an NA of 1.7. Here, we have used the CRLB to estimate the localization precision, but future work could benefit from implementing the Van Trees inequality [42] to take into account the prior knowledge of the fluorophores' locations. Finally, we note that in principle, TIRFscan can also be used with other PSF engineering methods or biplane axial localization methods, and that the PSF model used in this study is a Gaussian approximation and does not take into account effects such as supercritical angle fluorescence [43].

In summary, rapid sequential scanning of the TIRF angle within the “on” time of an emitter can increase the precision of its axial CRLB by a factor of approximately 2. Ideally, this can be done using prism or waveguide based TIRF where the critical angle can be achieved more precisely and optical back-reflections and scattering is minimized. For objective based TIRF, two angle scanning at the minimum and maximum possible TIRF angles shows clear axial localization improvement. The use of a NA = 1.7 objective can improve axial CRLB by a factor 3 while use of titanium oxide based waveguides can improve axial CRLB by a factor of 5–6 in the first 50 nm from the coverslip. This strategy can be combined with other schemes suitable for TIRF such as SIMFLUX [34] and direct photometry [30]. We foresee, that the precision and resolution gain in TIRF-based SMLM resulting from the here proposed technique will boost future single molecule studies.

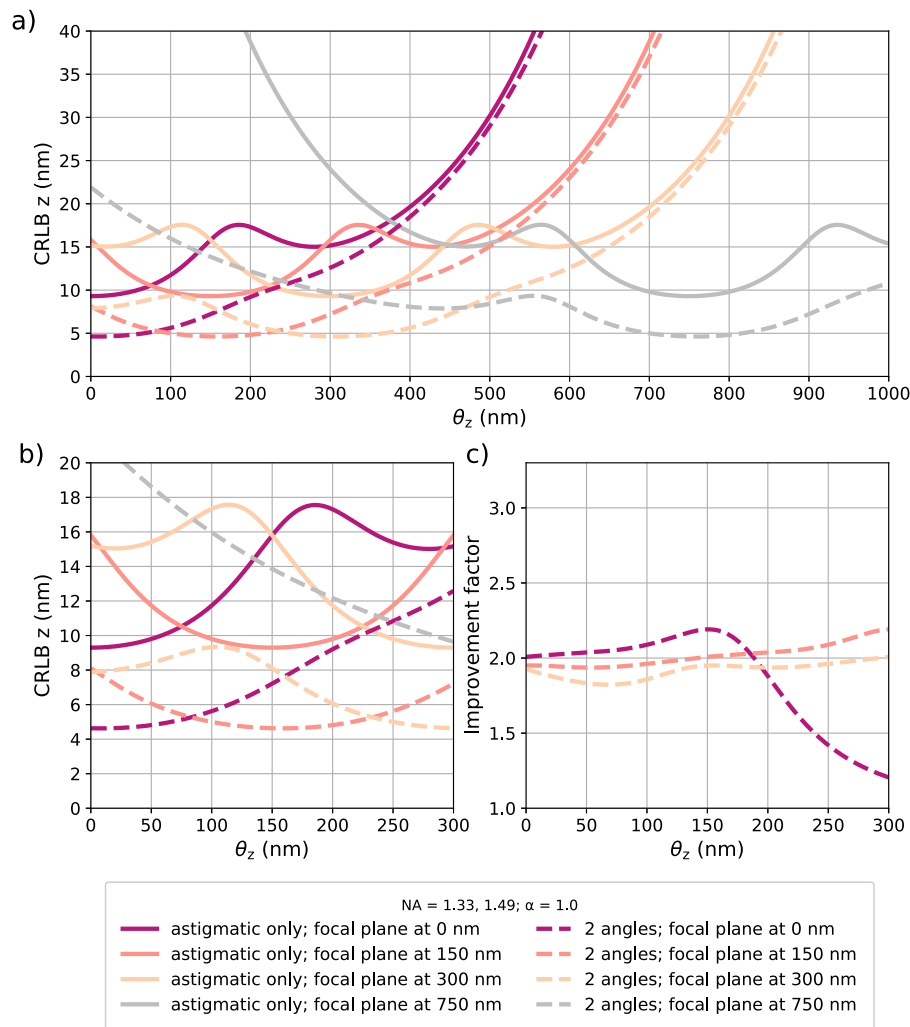


Fig. 4. TIRFscan CRLB and improvement factor for different focal plane positions (a) CRLB as the focal plane is moved away from the coverslip, (b) inset of CRLB, and (c) improvement factor for 2 TIRFscan angles (NA = 1.33, 1.49) with $\alpha = 1.0$ representing objective based TIRFscan with negligible scattering factor where the focal plane is placed at 0, 150, 300 and 750 nm above the coverslip. The intensity has been normalized, which in practice would mean adjusting laser power.

Declaration of competing interest

The authors declare the following financial interests/personal relationships which may be considered as potential competing interests: Carlos Smith reports financial support was provided by Dutch Research Council.

Carlos Smith reports administrative support was provided by Delft University of Technology.

Data availability

We have made the data available (see appendix).

Acknowledgments and disclosures

D.F. wishes to thank Sung Hyun Kim and Christiaan Hulleman for helpful discussions.

Funding

J.C, S.H., D.F. and C.S.S. were supported by the Netherlands Organisation for Scientific Research (NWO) under NWO START-UP project no. 740.018.015. N.H.D. was supported by funding from the Netherlands Organisation for Scientific Research (NWO) through Top grant

714.017.002, and from the European Research Council through an Advanced Grant (REPLI-CHROMA; grant number 789267). G.J.V. acknowledges support by the Dutch 4TU federation for the Plantenna project.

Appendix A. Supplementary data

Supplementary material related to this article can be found online at <https://doi.org/10.1016/j.optcom.2023.129548>. The Python code for calculating the CRLB of TIRFscan is provided on GitHub (<https://github.com/dfanology/TIRFscan>).

References

- [1] B. Huang, W. Wang, M. Bates, X. Zhuang, Three-dimensional super-resolution imaging by stochastic optical reconstruction microscopy, *Science* 319 (5864) (2008) 810–813, <http://dx.doi.org/10.1126/science.1153529>.
- [2] E. Betzig, G.H. Patterson, R. Sougrat, O.W. Lindwasser, S. Olenych, J.S. Bonifacino, M.W. Davidson, J. Lippincott-Schwartz, H.F. Hess, Imaging intracellular fluorescent proteins at nanometer resolution, *Science* 313 (5793) (2006) 1642–1645, <http://dx.doi.org/10.1126/science.1127344>.
- [3] M.J. Rust, M. Bates, X. Zhuang, Sub-diffraction-limit imaging by stochastic optical reconstruction microscopy (STORM), *Nature Methods* 3 (10) (2006) 793–796, <http://dx.doi.org/10.1038/nmeth929>.
- [4] F. Balzarotti, Y. Eilers, K.C. Gwosch, A.H. Gynnå, V. Westphal, F.D. Stefani, J. Elf, S.W. Hell, Nanometer resolution imaging and tracking of fluorescent molecules with minimal photon fluxes, *Science* 355 (6325) (2017) 606–612, <http://dx.doi.org/10.1126/science.aak9913>.

- [5] B. Huang, S.A. Jones, B. Brandenburg, Z. Zhuang, Whole-cell 3D STORM reveals interactions between cellular structures with nanometer-scale resolution, *Nature Methods* 5 (12) (2008) 1047–1052, <http://dx.doi.org/10.1038/nmeth.1274>.
- [6] L. Gu, Y. Li, S. Zhang, M. Zhou, Y. Xue, W. Li, T. Xu, W. Ji, Molecular-scale axial localization by repetitive optical selective exposure, *Nature Methods* 18 (4) (2021) 369–373, <http://dx.doi.org/10.1038/s41592-021-01099-2>.
- [7] G. Shtengel, J.A. Galbraith, C.G. Galbraith, J. Lippincott-Schwartz, J.M. Gillette, S. Manley, R. Sougrat, C.M. Waterman, P. Kanchanawong, M.W. Davidson, R.D. Fetter, H.F. Hess, Interferometric fluorescent super-resolution microscopy resolves 3D cellular ultrastructure, *Proc. Natl. Acad. Sci.* 106 (9) (2009) 3125–3130, <http://dx.doi.org/10.1073/pnas.0813131106>.
- [8] N. Karedla, A.M. Chizhik, S.C. Stein, D. Ruhlandt, I. Gregor, A.I. Chizhik, J. Enderlein, Three-dimensional single-molecule localization with nanometer accuracy using metal-induced energy transfer (MIET) imaging, *J. Chem. Phys.* 148 (20) (2018) 204201, <http://dx.doi.org/10.1063/1.5027074>.
- [9] D.W. Piston, G.-J. Kremers, Fluorescent protein FRET: The good, the bad and the ugly, *Trends Biochem. Sci.* 32 (9) (2007) 407–414, <http://dx.doi.org/10.1016/j.tibs.2007.08.003>.
- [10] S.J. Leavesley, T.C. Rich, Overcoming limitations of FRET measurements, *Cytometry A* 89 (4) (2016) 325–327, <http://dx.doi.org/10.1002/cyto.a.22851>.
- [11] G. Wang, J. Hauver, Z. Thomas, S.A. Darst, A. Pertsinidis, Single-molecule real-time 3D imaging of the transcription cycle by modulation interferometry, *Cell* 167 (7) (2016) 1839–1852.
- [12] P. Jouchet, C. Gabriel, N. Bourg, M. Bardou, C. Poüs, E. Fort, S. Lévêque-Fort, Nanometric axial localization of single fluorescent molecules with modulated excitation, *Nat. Photon.* 15 (4) (2021) 297–304, <http://dx.doi.org/10.1038/s41566-020-00749-9>.
- [13] P. Bon, J. Linarès-Loyez, M. Feyeux, K. Alessandri, B. Lounis, P. Nassoy, L. Cognet, Self-interference 3D super-resolution microscopy for deep tissue investigations, *Nature Methods* 15 (6) (2018) 449–454, <http://dx.doi.org/10.1038/s41592-018-0005-3>.
- [14] A.-K. Gustavsson, P.N. Petrov, M.Y. Lee, Y. Shechtman, W.E. Moerner, 3D single-molecule super-resolution microscopy with a tilted light sheet, *Nature Commun.* 9 (1) (2018) <http://dx.doi.org/10.1038/s41467-017-02563-4>.
- [15] S.-T. Hung, J. Cnossen, D. Fan, M. Siemons, D. Jurriens, K. Grusmayer, O. Soloviev, L.C. Kapitein, C.S. Smith, SOLEIL: single-objective lens induced light sheet localization microscopy, *Biomed. Opt. Express* 13 (6) (2022) 3275, <http://dx.doi.org/10.1364/boe.451634>.
- [16] M. Heilemann, S. van de Linde, M. Schüttelz, R. Kasper, B. Seefeldt, A. Mukherjee, P. Tinnefeld, M. Sauer, Subdiffraction-resolution fluorescence imaging with conventional fluorescent probes, *Angew. Chem. Int. Ed.* 47 (33) (2008) 6172–6176, <http://dx.doi.org/10.1002/anie.200802376>.
- [17] S. Yamada, W.J. Nelson, Localized zones of rho and rac activities drive initiation and expansion of epithelial cell–cell adhesion, *J. Cell Biol.* (ISSN: 0021-9525) 178 (3) (2007) 517–527, <http://dx.doi.org/10.1083/jcb.200701058>, [arXiv:https://rupress.org/jcb/article-pdf/178/3/517/1331236/jcb.200701058.pdf](https://rupress.org/jcb/article-pdf/178/3/517/1331236/jcb.200701058.pdf).
- [18] A.B. Jaykumar, P.S. Caceres, I. Sablaban, B.A. Tannous, P.A. Ortiz, Real-time monitoring of NKCC2 endocytosis by total internal reflection fluorescence (TIRF) microscopy, *Am. J. Physiol.-Renal Physiol.* 310 (2) (2016) F183–F191, <http://dx.doi.org/10.1152/ajprenal.00104.2015>, [arXiv:https://doi.org/10.1152/ajprenal.00104.2015](https://doi.org/10.1152/ajprenal.00104.2015), PMID: 26538436.
- [19] I. Akopova, S. Tatur, M. Grygorczyk, R. Luchowski, I. Gryczynski, Z. Gryczynski, J. Borejdo, R. Grygorczyk, Imaging exocytosis of ATP-containing vesicles with TIRF microscopy in lung epithelial A549 cells, *Purinergic Signal.* 8 (1) (2012) 59–70, <http://dx.doi.org/10.1007/s11302-011-9259-2>.
- [20] R.L. Webb, O. Rozov, S.C. Watkins, B.M. McCartney, Using total internal reflection fluorescence (TIRF) microscopy to visualize cortical actin and microtubules in the drosophila syncytial embryo, *Dev. Dyn.* 238 (10) (2009) 2622–2632, <http://dx.doi.org/10.1002/dvdy.22076>.
- [21] W.P. Ambrose, P.M. Goodwin, J.P. Nolan, Single-molecule detection with total internal reflection excitation: comparing signal-to-background and total signals in different geometries, *Cytometry* 36 (3) (1999) 224–231, [http://dx.doi.org/10.1002/\(SICI\)1097-0320\(19990701\)36:3<224::AID-CYTO12>3.0.CO;2-J](http://dx.doi.org/10.1002/(SICI)1097-0320(19990701)36:3<224::AID-CYTO12>3.0.CO;2-J).
- [22] A. Priyadarshi, F.T. Dullo, D.L. Wolfson, A. Ahmad, N. Jayakumar, V. Dubey, J.-C. Tinguely, B.S. Ahluwalia, G.S. Murugan, A transparent waveguide chip for versatile total internal reflection fluorescence-based microscopy and nanoscopy, *Commun. Mater.* 2 (1) (2021) 85, <http://dx.doi.org/10.1038/s43246-021-00192-5>.
- [23] M. Brunstein, M. Teremetz, K. Hérault, C. Tourain, M. Oheim, Eliminating unwanted far-field excitation in objective-type TIRF. Part I. Identifying sources of nonevanescent excitation light, *Biophys. J.* 106 (5) (2014) 1020–1032, <http://dx.doi.org/10.1016/j.bpj.2013.12.049>.
- [24] K. Kwakwa, A. Savell, T. Davies, I. Munro, S. Parrinello, M.A. Purbhoo, C. Dunsby, M.A. Neil, P.M. French, Easystorm: a robust, lower-cost approach to localisation and tirf microscopy, *J. Biophotonics* 9 (9) (2016) 948–957, <http://dx.doi.org/10.1002/jbio.201500324>, [arXiv:https://onlinelibrary.wiley.com/doi/pdf/10.1002/jbio.201500324](https://onlinelibrary.wiley.com/doi/pdf/10.1002/jbio.201500324).
- [25] H. Shen, E. Huang, T. Das, H. Xu, M. Ellisman, Z. Liu, TIRF microscopy with ultra-short penetration depth, *Opt. Express* 22 (9) (2014) 10728, <http://dx.doi.org/10.1364/OE.22.010728>.
- [26] F. Lanni, A.S. Waggoner, D.L. Taylor, Structural organization of interphase 3t3 fibroblasts studied by total internal reflection fluorescence microscopy, *J. Cell Biol.* 100 (4) (1985) 1091–1102, <http://dx.doi.org/10.1083/jcb.100.4.1091>, [arXiv:https://rupress.org/jcb/article-pdf/100/4/1091/1051400/1091.pdf](https://rupress.org/jcb/article-pdf/100/4/1091/1051400/1091.pdf).
- [27] A. Rohrbach, Observing secretory granules with a multiangle evanescent wave microscope, *Biophys. J.* 78 (5) (2000) 2641–2654, [http://dx.doi.org/10.1016/S0006-3495\(00\)76808-1](http://dx.doi.org/10.1016/S0006-3495(00)76808-1).
- [28] W. Sun, K. Marchuk, G. Wang, N. Fang, Autocalibrated scanning-angle prism-type total internal reflection fluorescence microscopy for nanometer-precision axial position determination, *Anal. Chem.* 82 (6) (2010) 2441–2447, <http://dx.doi.org/10.1021/ac902789z>, [arXiv:https://doi.org/10.1021/ac902789z](https://doi.org/10.1021/ac902789z).
- [29] M.C.D. Santos, R. Déturche, C. Vézy, R. Jaffiol, Topography of cells revealed by variable-angle total internal reflection fluorescence microscopy, *Biophys. J.* 111 (6) (2016) 1316–1327,